water

MDPI

Article

Turbulent Flow Through Sluice Gate and Weir Using Smoothed Particle Hydrodynamics: Evaluation of Turbulence Models, Boundary Conditions, and 3D Effects

Efstathios Chatzoglou and Antonios Liakopoulos *

Hydromechanics and Environmental Engineering Laboratory, Department of Civil Engineering, University of Thessaly, Pedion Areos, 38334 Volos, Greece; efchatzoglou@uth.gr
* Correspondence: aliakop@uth.gr

Abstract: Understanding flow dynamics around hydraulic structures is essential for optimizing water management systems and predicting flow behavior in real-world applications. In this study, we simulate a 3D flow control system featuring a sluice gate and a weir, commonly used in hydraulic engineering. The focus is on accurately incorporating modified dynamic boundary conditions (mDBCs) and viscosity treatment to improve the simulation of complex, turbulent flows. We assess the performance of the Smoothed Particle Hydrodynamics (SPH) method in handling these challenging conditions. Especially when the boundary conditions and applicability to industry are two of the SPH method's grand challenges. Simulations were conducted on a Graphics Processing Unit (GPU) using the DualSPHysics code. The results were compared to theoretical predictions and experimental data found in the literature. Key hydraulic characteristics, including 3D flow effects, hydraulic jump formation, and turbulent behavior, are examined. The combination of mDBCs with the Laminar plus sub-particle scale turbulence model achieved the correct simulation results. The findings demonstrate agreement between simulations, theoretical predictions, and experimental results. This work provides a reliable framework for analyzing turbulent flows in hydraulic structures and can be used as reference data or a prototype for larger-scale simulations in both research and engineering design, particularly in contexts requiring robust and precise flow control and/or environmental management.

Keywords: sluice gate; hydraulic jump; boundary conditions; mDBCs; smoothed particle hydrodynamics (SPH); flow control system

check for updates

Academic Editor: Georg Umgiesser

Received: 9 December 2024
Revised: 5 January 2025
Accepted: 6 January 2025
Published: 8 January 2025

Citation: Chatzoglou, E.; Liakopoulos, A. Turbulent Flow Through Sluice Gate and Weir Using Smoothed Particle Hydrodynamics: Evaluation of Turbulence Models, Boundary Conditions, and 3D Effects. *Water* **2025**, *17*, 152. https://doi.org/10.3390/w17020152

Copyright: © 2025 by the authors. Licensee MDPI, Basel, Switzerland. This article is an open access article distributed under the terms and conditions of the Creative Commons Attribution (CC BY) license (https://creativecommons.org/licenses/by/4.0/).

1. Introduction

Water management and the related hydraulic structures play a vital role in societies, offering numerous advantages like irrigation, flood management, water supply, and hydroelectric power production [1]. Sluice gates and weirs are extensively utilized in hydraulic engineering to regulate and monitor water levels in canals, rivers, and reservoirs. A comprehensive understanding of how water flows over, under, and around these structures is essential for designing effective and safe hydraulic systems.

Experimental approaches have been the primary methods for investigating water flow around, over, and beneath hydraulic structures. While effective, these techniques can be time-consuming, can be costly, and may fall short in capturing the complex dynamics, such as intricate flow patterns, present in real-world hydraulic systems [2]. With advances in computer technology, numerical simulation methods like Computational Fluid Dynamics (CFD) have become increasingly favored for analyzing fluid flow in hydraulic structures.

Reynolds Averaged Navier–Stokes (RANS) is frequently used in engineering applications due to its lower computational cost, as it solves the time-averaged Navier–Stokes equations with turbulence models like k-ε, k-ω, Spalart–Allmaras model, etc., to account for turbulence effects. Additionally, particle-based methods such as Molecular Dynamics (MD) [3], Dissipative Particle Dynamics (DPD) [4], and Smooth Dissipative Particle Dynamics (SDPD) [5] offer alternative approaches for simulating fluid flow at small scales.

Among these techniques, Smoothed Particle Hydrodynamics (SPH) has emerged as a powerful tool in microflow simulations of large engineering systems. SPH models liquids as a set of mass points, "particles", which act as moving computational nodes to solve the partial differential equations (PDEs) governing fluid motion [6]. The method offers distinct advantages, particularly in handling free surface flows, moving boundaries, and flows with significant deformations making it a highly effective solution for complex fluid flow simulations [7]. Several studies have successfully applied the SPH method. Some of them studied effectively wave impacts on offshore and coastal structures, even with floating objects [8–10], flow over river waterworks [11], applications on multiphase flows [12,13], closed channel flows [14–17], etc.

In research related to the present study, Chatzoglou and Liakopoulos [18] simulated a 3D sluice gate–weir system, achieving results close to experimental data and theoretical analysis. However, unexpected particle behavior was observed close to the vertical solid walls. In a later study, Zhang et al. [19] studied the fluid–structure interaction problem involving structural movement and deformation with the SPH method. Their numerical results were in good agreement with experimental data regarding the flow pattern of the water and the behavior of the elastic sluice gate. Another study on fluid–structure interaction was conducted by Martnez-Estevez et al. [20]. In their study, they used a coupled SPH-based solver and Finite Element Analysis (FEA) for simulation of an elastic sluice gate. Their results were validated with reference cases and proved that their models were as accurate as other approaches presented in the literature.

Despite its proven effectiveness in simulating open channel flows, the SPH method still faces limitations, which are categorized in convergence, consistency, and stability; boundary conditions; adaptivity; coupling to other models; and applicability to industry [21]. It is obvious that there is a need for more sophisticated boundary conditions.

Several approaches have been proposed in the literature to enforce solid boundaries. One approach is using the method of repulsive forces [22,23], yet the accuracy of SPH spatial interpolation close to the solid walls is reduced. Another option is to discretize the boundaries with the so-called semi-analytical formulation [24–26]. A third way is based on fictitious particles to fill the space beyond the boundary interface to mimic the solid wall [27–30]. This third option is based on the modified dynamic boundary conditions (mDBCs) introduced by English et al. [31]. Using them can alleviate limitations such as dissipation and unphysical values of density and pressure close to the solid boundaries. The main idea behind mDBCs is that the density of solid particles is obtained from positions within the fluid domain (ghost nodes) by linear extrapolation. For their use to reach its highest potential, it should be handled carefully. More about the mDBCs can be found in Section 2.2.

In this study, we simulate a 3D flow control system with a sluice gate and a weir at the outlet. Emphasis is given to the most appropriate incorporation of the mDBCs and turbulence modeling. The results are compared with theoretical equations retrieved from the literature and the experimental data of [32]. In addition, 3D effects and hydraulic characteristics of the flow are highlighted. The main objective is to assess the SPH method in highly turbulent 3D flows handling the existing BCs in the most efficient way. All simulations run on GPU through the DualSPHysics code [33].

The results are in good agreement with the experimental data and the theoretical solutions, and thus, our models can be used as reference data or prototype for larger scale simulations.

2. Governing Equations and Solution Methodology

The governing equations describe the simultaneous evolution of ρ (density) and v (velocity). In the context of the weakly compressible formulation, they are expressed as

$$\frac{d\rho}{dt} = -\rho\,\nabla\cdot\boldsymbol{v} \tag{1}$$

$$\frac{d\boldsymbol{v}}{dt} = -\frac{1}{\rho}\nabla P + \boldsymbol{g} + \boldsymbol{\Gamma} \tag{2}$$

where P is the pressure, **g** represents the external force per unit mass, and **Γ** represents the sum of all dissipative terms in the momentum equation.

2.1. SPH Formulation of the Governing Equations

In the SPH framework, an arbitrary time-dependent scalar field A is expressed as

$$A(r,t) = \int A(r',t)\,\delta(r-r',h)\,dr' \tag{3}$$

where r and r' represent "particle" positions, h is the "smoothing length", and δ is Dirac's delta function. The δ-Dirac distribution is approximated by an interpolation kernel W. It follows that, e.g., for a time independent field,

$$A_1(r) = \int A(r')\,W(r-r',h)\,dr' \tag{4}$$

As outlined by Monaghan [34] and Liu [35], the smoothing kernel must satisfy several key properties. These properties include compact support, normalization, positivity within a defined interaction zone, a monotonically decreasing value with distance, and differentiability; for example, see Monaghan [36]. The normalization requirement is expressed as

$$\int W(r-r',h)\,dr' = 1. \tag{5}$$

Furthermore,

$$\lim_{h\to 0} W(r-r',h) = \delta(r-r') \tag{6}$$

For numerical work, we replace the integral by summation over all particles:

$$A_s(r) = \sum_b m_b \frac{A_b}{\rho_b} W(r-r_b,h) \tag{7}$$

where m_b and ρ_b are the mass and density of particle b, respectively.

Several types of kernel functions can be used, each with its advantages, yet for the simulations conducted in this study, the Wendland's kernel function is adopted [37]. The choice of Wendland's kernel is based on the author's previous experience and is given by

$$W(\boldsymbol{r},h) = a_D\left(1-\frac{q}{2}\right)^4(2q+1) \quad if\ 0 \le q \le 2 \tag{8}$$

where a_D is equal to $7/(4\pi h^2)$ in 2D and $21/(16\pi h^3)$ in 3D and q = r/h.

The conservation of mass equation and momentum equation are approximated as

$$\frac{d\rho_i}{dt} = \rho_i \sum_j \frac{m_j}{\rho_j} \boldsymbol{v}_{ij} \cdot \nabla_i W_{ij} \tag{9}$$

$$\frac{d\boldsymbol{v}_i}{dt} = -\sum_j m_j \left(\frac{P_j + P_i}{\rho_j \rho_i} \right) \nabla_i W_{ij} + \boldsymbol{g} + \sum_j m_j \left(\frac{4\nu_0 \boldsymbol{r}_{ij} \cdot \nabla_i W_{ij}}{(\rho_i + \rho_j)\left({r_{ij}}^2 + \eta^2\right)} \right) v_{ij} + \boldsymbol{\Gamma}_2 \tag{10}$$

where ν_0 is the kinematic viscosity, m_j, ρ_j are the mass and density of particle j, and $\boldsymbol{\Gamma}_2$ represents the remaining dissipation term [33].

In the DualSPHysics code, there are two options regarding the viscosity treatment of the flow. The artificial viscosity treatment and the Laminar + SPS (sub-particle scale). In the remainder of the paper, we will refer to artificial viscosity as (AVM) and to Laminar + SPS as L-SPS.

The artificial viscosity treatment is a common option in many simulations due to its simplicity. It should be noted that artificial viscosity does not represent the physical viscosity of the fluid, but it is a means to calculate the flow dissipation [34].

The momentum equation takes the form

$$\frac{d\boldsymbol{v}_i}{dt} = -\sum_j m_j \left(\frac{P_j + P_i}{\rho_j \rho_i} + \Pi_{ij} \right) \nabla_i W_{ij} + \boldsymbol{g} \tag{11}$$

where in Equation (11), the term Π_{ij} is given by

$$\Pi_{ij} = \begin{cases} -\frac{a \bar{c}_{ij} \mu_{ij}}{\rho_{ij}} & \boldsymbol{v}_{ij} \cdot \boldsymbol{r}_{ij} < 0 \\ 0 & \boldsymbol{v}_{ij} \cdot \boldsymbol{r}_{ij} > 0 \end{cases} \tag{12}$$

where $\bar{c}_{ij}$ is the mean speed of sound and α is a coefficient that needs to be tuned in order to introduce the proper dissipation. A value of $a = 0.01$ has proven to give satisfactory results in many cases of free surface flows [38].

In Equation (12),

$$\mu_{ij} = \frac{h \boldsymbol{v}_{ij} \cdot \boldsymbol{r}_{ij}}{{r_{ij}}^2 + \eta^2}$$

where $\eta^2 = 0.01h^2$.

With the Laminar + SPS (L-SPS), the conservation of momentum equation takes the form

$$\frac{d\boldsymbol{v}_i}{dt} = -\sum_j m_j \left(\frac{P_j + P_i}{\rho_j \rho_i} \right) \nabla_i W_{ij} + \boldsymbol{g} + \sum_j m_j \left(\frac{4\nu_o r_{ij} \cdot \nabla_i W_{ij}}{(\rho_i + \rho_j)\left({r_{ij}}^2 + \eta^2\right)} \right) \boldsymbol{v}_{ij} + \sum_j m_j \left(\frac{\vec{\tau}_{\alpha\beta}{}^j}{{\rho_j}^2} + \frac{\vec{\tau}_{\alpha\beta}{}^i}{{\rho_i}^2} \right) \nabla_i W_{ij} \tag{13}$$

where the indices take the value $\alpha = 1, 2, 3$ and $\beta = 1, 2, 3$. The sub-particle scale stress tensor, denoted as $\vec{\tau}$, is computed analogously to the Standard Smagorinsky approach [39].

The pressure is given by the Tait's equation of state:

$$P = B \left[\left(\frac{\rho}{\rho_0} \right)^{\gamma} - 1 \right] \tag{14}$$

where $\rho_0 = 1000\ \mathrm{kg/m^3}$ is the reference water density, $\gamma = 7$, $B = \frac{{c_s}^2 \rho_o}{\gamma}$, and c_s represents the speed of sound. The speed of sound should be usually given a value of 10 times the maximum velocity value of the flow system in order to limit density variations [33].

2.2. Treatment of Fluid/Solid Boundary Conditions

In this work, an important role on the quality of the simulation data plays the correct use of the modified dynamic boundary conditions (mDBCs) proposed by English et al. [31]. In this implementation, boundary particles are positioned similarly to those in the original dynamic boundary conditions (DBCs), with the boundary interface located half a particle spacing away from the innermost layer of boundary particles. For each boundary particle, a ghost node is projected into the fluid across the boundary interface, following a method analogous to Marrone et al. [28]. On a flat surface, the ghost node is mirrored across the boundary interface along the direction of the boundary normal that points into the fluid (see Figure 1), and the fluid properties at this ghost node are determined using a corrected SPH sum of the surrounding fluid particles. In the case of a boundary particle at a corner, using the boundary normal is ineffective due to the presence of multiple normal vectors. Instead, the boundary interfaces of each solid boundary converge to form a corner, and the ghost node is mirrored through this corner point into the fluid region (Figure 1). Similarly, fluid properties at the ghost node are obtained via a corrected SPH sum of the surrounding fluid.

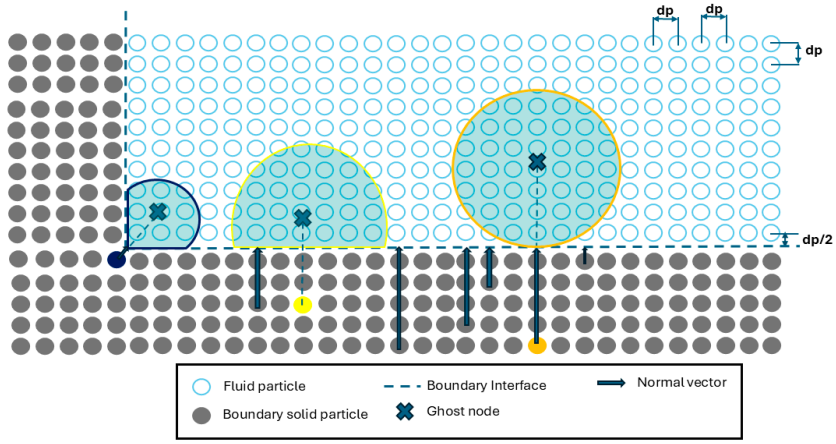


Figure 1. mDBC representation. The mirroring of ghost nodes (crosses) and the kernel radius around the ghost nodes for boundary particles in a flat surface and a corner.

The boundary particles receive fluid properties using the values calculated at the ghost node and an extrapolation method like the one used for open boundaries [40]. The density of the boundary particle ρ_b and the ghost particle ρ_g and its gradients are computed at the ghost node using the first-order SPH interpolation proposed by Liu and Liu [41]. This requires solving the following linear system for each ghost node:

$$\boldsymbol{A}_g \cdot \begin{bmatrix} \rho_g \\ \partial_x \rho_g \\ \partial_y \rho_g \\ \partial_z \rho_g \end{bmatrix} = \boldsymbol{b}_g \tag{15}$$

$$\boldsymbol{A}_g = \begin{bmatrix} \sum_j W_{gj} V_j & \sum_j (x_j - x_g) W_{ij} V_j & \sum_j (y_j - y_g) W_{gj} V_j & \sum_j (z_j - z_g) W_{gj} V_j \\ \sum_j \partial_x W_{gj} V_j & \sum_j (x_j - x_g) \partial_x W_{ij} V_j & \sum_j (y_j - y_g) \partial_x W_{gj} V_j & \sum_j (z_j - z_g) \partial_x W_{gj} V_j \\ \sum_j \partial_y W_{gj} V_j & \sum_j (x_j - x_g) \partial_y W_{ij} V_j & \sum_j (y_j - y_g) \partial_y W_{gj} V_j & \sum_j (z_j - z_g) \partial_y W_{gj} V_j \\ \sum_j \partial_z W_{gj} V_j & \sum_j (x_j - x_g) \partial_z W_{ij} V_j & \sum_j (y_j - y_g) \partial_z W_{gj} V_j & \sum_j (z_j - z_g) \partial_z W_{gj} V_j \end{bmatrix} \tag{16}$$

and

$$\boldsymbol{b}_g{}^T = [\sum_j W_{gj} m_j \ \sum_j \partial_x W_{gj} m_j \ \sum_j \partial_y W_{gj} m_j \ \sum_j \partial_z W_{gj} m_j \ ] \quad (17)$$

where in Equations (15)–(17), the subscript g refers to the ghost node, while j refers to the neighboring fluid particle.

3. SPH Model Construction and Simulation Results

To assess the effectiveness of the SPH method in simulating rapidly varying flows, such as the flow under a sluice gate and the formation of a hydraulic jump, several numerical experiments were conducted. All cases were run on GPU utilizing an RTX 3080 GPU card.

3.1. Geometry and SPH Model Construction

The hydraulic system geometry parameters were chosen to conform with the experimental setup of [32] for comparison. The length of the channel was 6.14 m and its width 15 cm. The initial upstream water depth was set at Y_u = 20 cm. The sluice gate was placed at X = 2.02 m (see Figure 2), while a weir was placed at the computational domain outlet (X = 6.14 m). Symbols used for various lengths are included in Figure 2.

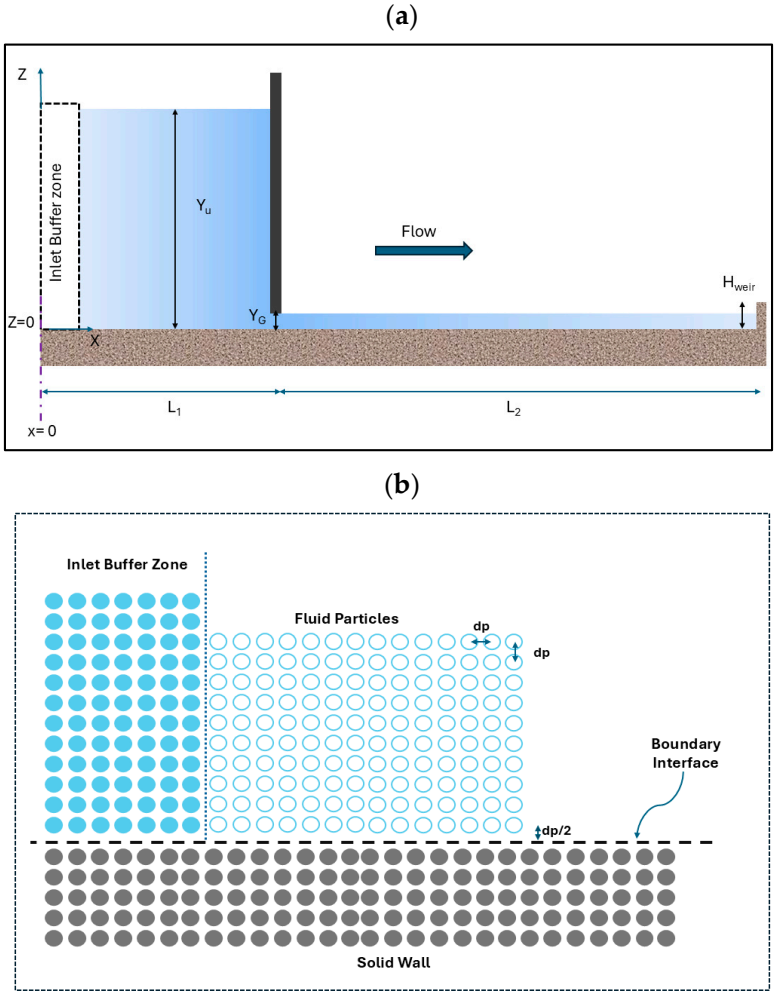


Figure 2. Simulation model set up. (**a**) L_1 = 2.02 m, L_2 = 4.12, H_{weir} = the height of the weir depending on the case, Y_U = upstream initial water depth = 20 cm, and Y_G = 0.025 m is the gate opening; (**b**) solid wall particles and the initial arrangement of liquid particles.

In the present work, particular emphasis was given to the boundary condition treatment. Inlet/outlet boundary conditions were applied in the streamwise direction, while

for the imposition of liquid/solid boundaries, the modified dynamic boundary conditions (mDBCs) [31] were used. In the inlet buffer zone, the water depth and velocity were kept constant in order to achieve a constant volume flowrate.

Given the small gate opening (Y_G = 0.025 m), the initial interparticle distance (dp) was chosen to ensure that enough particles passed through the sluice gate. Thus, the value of dp = 0.005 m was chosen with a h/dp = 1.5 to be the most effective ratio of smoothing length over the initial interparticle length.

3.2. Physical Models

Two physical models were considered for the computation of the flow dissipation: the artificial viscosity model (AVM) [33] and the Laminar plus sub-particle scale (L-SPS) model [39]. Both models were briefly described in Section 2.1.

One important simulation parameter is the so called "ViscoBound" (VB) factor. This parameter relates the viscosity of the fluid with the viscosity of the fluid at the liquid/solid interface.

When the artificial viscosity was used, the parameter α (see Equation (12)) tuned the viscosity of the fluid while α_{BF} the viscosity at the liquid/solid interface. The two parameters were related through $\alpha_{BF} = \alpha \times$ VB [33].

When the L-SPS model was selected, the kinematic viscosity was set equal to $\nu_0 = 10^{-6}$ m^2/s for water. The simulation parameters of each case can be found in Table 1.

Table 1. Key simulation parameters.

Case	Y_G (m)	Y_U (m)	H_{weir} (m)	N_p	Density (kg/m^3)	Physical Model	Simulation Time (s)
AVM	0.025	0.20	0.025	2057327	1000	Artificial visc.	200
L-SPS	0.025	0.20	0.025	2057327	1000	Laminar + SPS	200

Both AVM and L-SPS are embedded options in the DualSPHysics code. The artificial viscosity model often smooths turbulence features, while the L-SPS model captures essential turbulent structures more effectively. The comparison shed light on each model's suitability for complex hydraulic flows depending on the accuracy level desired.

3.3. Presentation of the SPH Results

Keeping the hydraulic system geometry fixed, two major families of simulations were conducted in order to compare the performance of the two models. The key simulation parameters in the two groups of simulations are listed in Table 1. Within each family of simulations, the effect of the parameter VB was studied.

3.3.1. Artificial Viscosity Model (AVM)

Three VB factor values (VB 1, 10, and 100) were examined. The differences between them were related mainly to the location of the formation of the hydraulic jump and the formation of coherent flow structures, mainly upstream from the sluice gate. In Figure 3, we present the most effective result in capturing the coherent structures, i.e., for VB = 100. The conditions downstream of the sluice gate were clearly free-flow conditions. The jump formed immediately after the gate at X = 2.06 m. Figure 3 depicts the development of the flow in time, the formation of the hydraulic jump, and the magnitude of the x-component of velocity downstream of the sluice gate.

In addition to the flow under the sluice gate and the formation of the hydraulic jump, it was important in order to assess the performance of SPH to capture coherent flow structures, such as vortices upstream of the sluice gate. Roth and Hager, based on experimental observations, presented a definition sketch for the flow near a standard gate with edge vortices. The sketch is redrawn in Figure 4, using the symbols of the present paper.

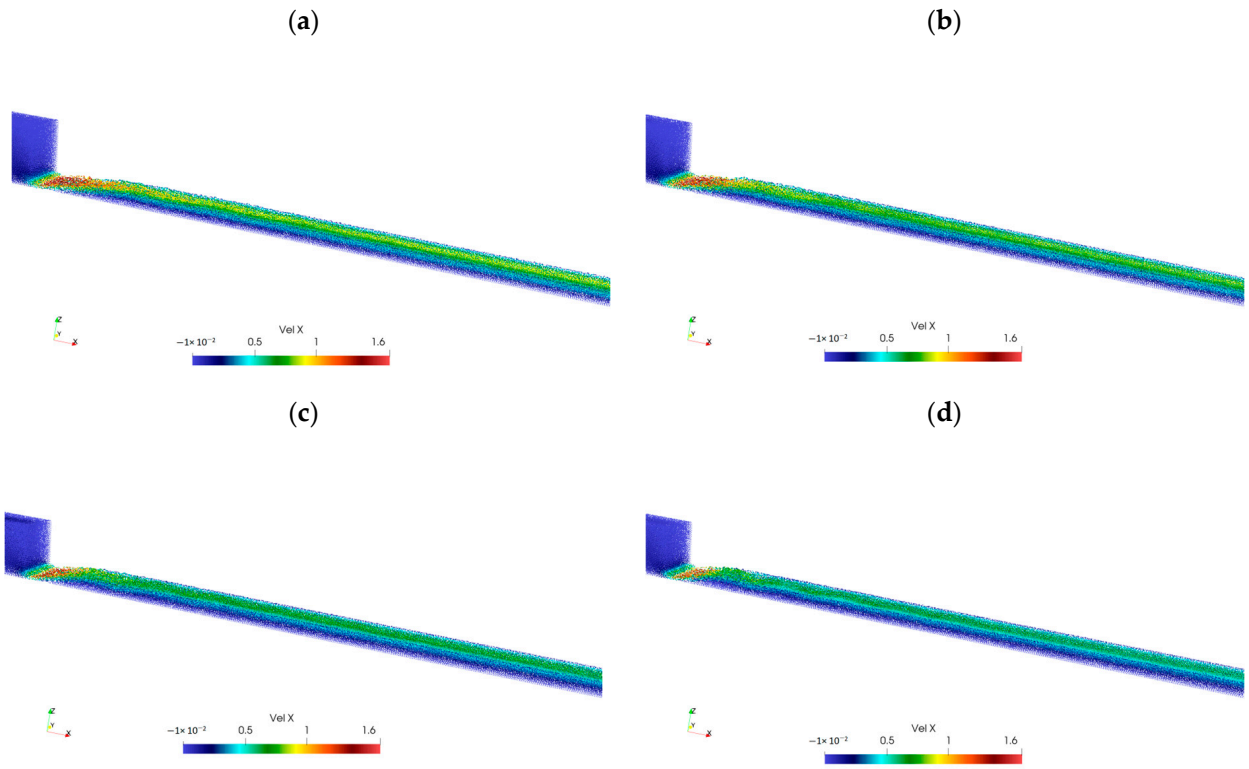


Figure 3. AVM. The transient formation of the hydraulic jump. (**a**) T = 50 s, (**b**) T = 100 s, (**c**) T = 150 s, (**d**) T = 200 s.

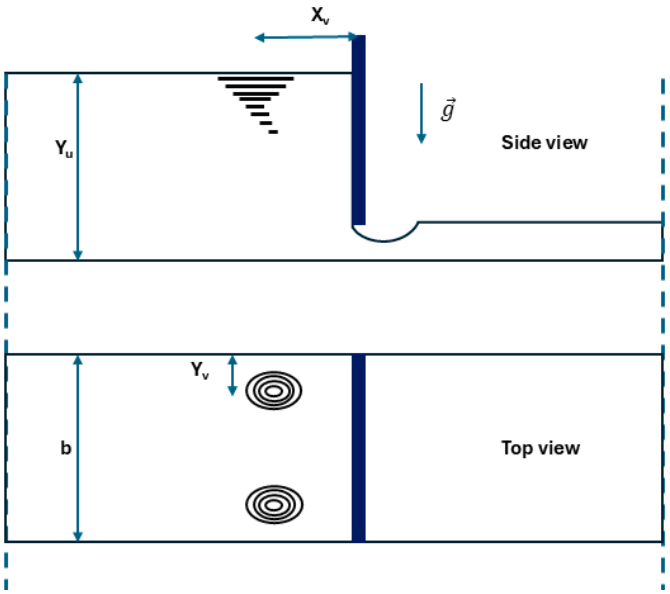


Figure 4. The definition sketch for corner vortices upstream of the sluice gate (from [42]).

As it was documented experimentally in [42], two symmetrical vortices were formed at the edge of the gate.

These vortices were clearly observed in our SPH simulation. The time evolution of the vortex formation in the SPH simulation near the water free surface (at Z = 18 cm) is depicted in Figure 5.

The SPH model demonstrated a clear capability to capture the coherent flow structures detailed in [42]. However, it was essential to validate these results by comparing them with the experimental findings of Roth and Hager. Their research involved a series of

experiments conducted in a channel measuring 500 mm, 350 mm, and 245 mm in width and 7 m in length. They derived the following expressions for distances along the X-axis (streamwise) and Y-axis (spanwise), in which vortices are formed. Their expressions for x_v and y_v are as follows:

$$x_v = \frac{1}{2}A^{-0.75}, \quad y_v = \frac{2}{3}\exp(-3Y_G) \tag{18}$$

where A is the relative gate opening (Y_G/Y_U) and $x_v = \frac{X_v}{Y_G}, y_v = \frac{Y_v}{Y_G}$.

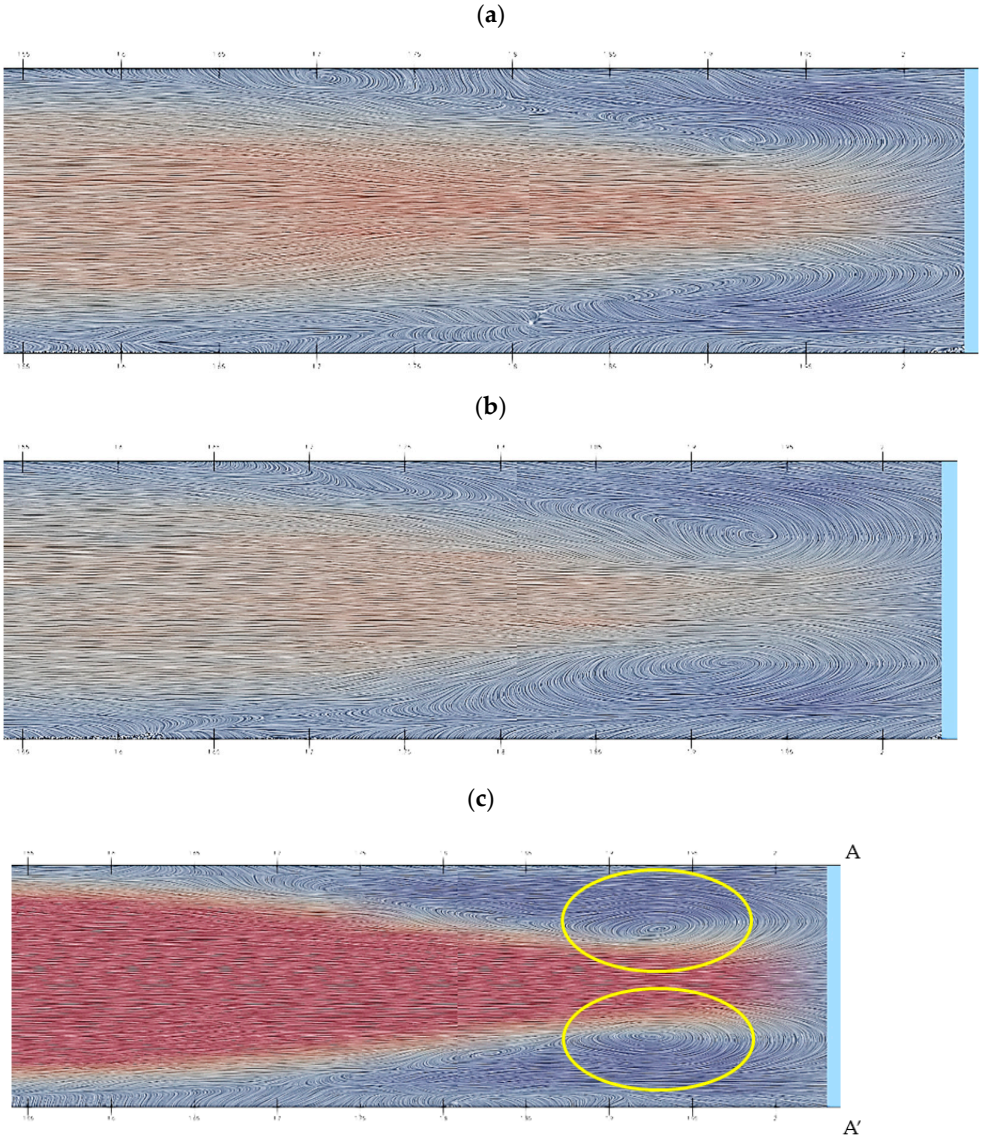


Figure 5. AVM. The transient formation of the coherent vortices upstream of the sluice gate, as seen on a horizontal plane at Z = 18 cm, (**a**) T = 100 s, (**b**) T = 150 s, (**c**) T = 200 s. AA′ sluice gate.

For the present hydraulic system geometry, the anticipated values from Equation (18) were X_v = 0.06 m and Y_v = 0.016 m. In the SPH results, the centers of the vortices were located at $X_{v\text{-SPH}}$ = 0.08 m and $Y_{v\text{-SPH}}$ = 0.04 m. It should be noted that the channel width in our simulations was narrower than the ones used in the experiments. In their research, [42] mention that the vortex is closer to the wall for a wide channel than for a narrow channel.

The flow is in a transient state for about 120 s. Time series plots correspond at points upstream of the sluice gate: point (X = 1.81 m, Y = 0.075 m, Z = 0.005 m), point (X = 1.81 m, Y = 0.075 m, Z = 0.14 m), and (X = 1.81 m, Y = 0.075 m, Z = 0.18 m); see Figure A1. They correspond downstream from the sluice gate and beyond the influence of hydraulic jump

at point (X = 3 m, Y = 0.075 m, Z = 0.005 m), point (X = 3 m, Y = 0.075 m, Z = 0.035), and (B3, X = 3 m, Y = 0.075 m, Z = 0.05 m); see Figure A2 in Appendix A. Figures 6 and 7 illustrate color-coded velocity distribution at cross-sections X = 1.81 m and X = 3m, respectively. The velocity distribution is as expected qualitatively in both cross-sections.

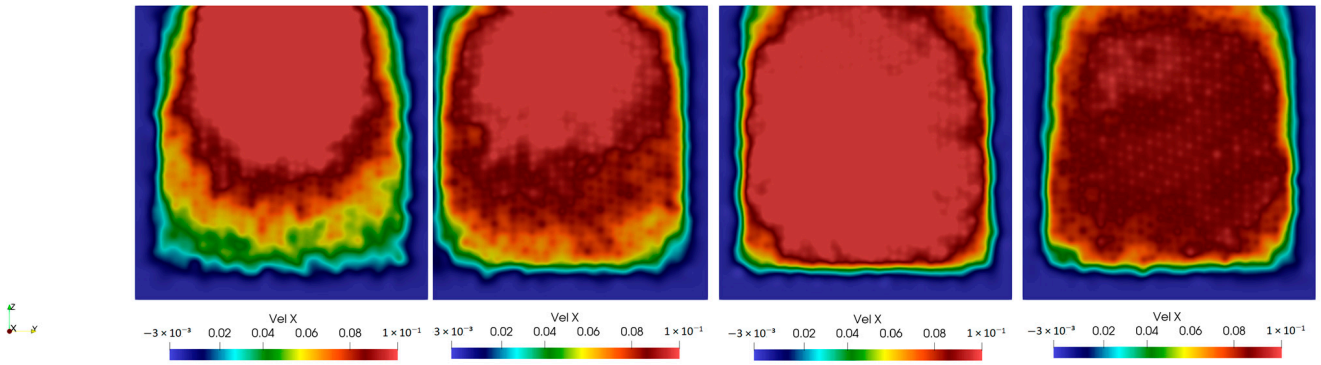


Figure 6. AVM. X-component of velocity. Front view. X = 1.81 m. Snapshots at T = 50, T = 100, T = 150, T = 200 s.

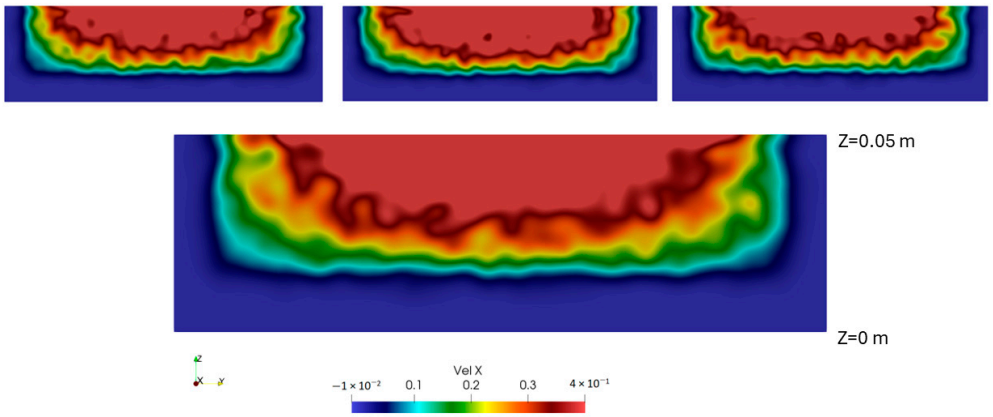


Figure 7. AVM. X-component of velocity. Front view. X = 3 m. Snapshots at T = 50, T = 100, T = 150, T = 200 s.

Mass conservation was satisfied as expected in an effective SPH simulation. We note here that excluding the possibility of liquid particles exiting the computational domain through the channel solid walls (due to inappropriate parameter selection or inadequate design of the solid walls), the mass conservation principle was satisfied automatically due to the fixed number of fluid particles in the simulations. The volume flow rate and the mean velocity value for each location are presented in Table 2.

Table 2. AVM (Q_{inlet} = 2.5 L/s). The mean velocity and water depth at the selected cross-sections. Here, h is the water depth at a cross-section.

V_{1_81} = 0.093 m/s	V_{2_05} = 0.9 m/s	V_3 = 0.336 m/s
h_{1_81} = 0.18 m	h_{2_05} = 0.0187 m	h_3 = 0.05 m
q_{1_81} = 0.0168 m^2/s	q_{2_05} = 0.0168 m^2/s	q_3 = 0.0168 m^2/s

Velocity profiles at selected longitudinal positions on the channel vertical midplane (Y = 0.075 m) are shown in Figure 8.

The hydraulic jump was formed a few centimeters downstream of the sluice gate. A series of small rollers developed on the surface. Further downstream, the water surface remained relatively smooth (Figure 9). These macroscopic characteristics of the SPH prediction classified the jump as a weak jump. We noted that the Froude number upstream of

the jump was equal to Fr_1 = 2.1, and a weak jump was expected according to experimental observations in wide channels available in the standard hydraulics literature [43].

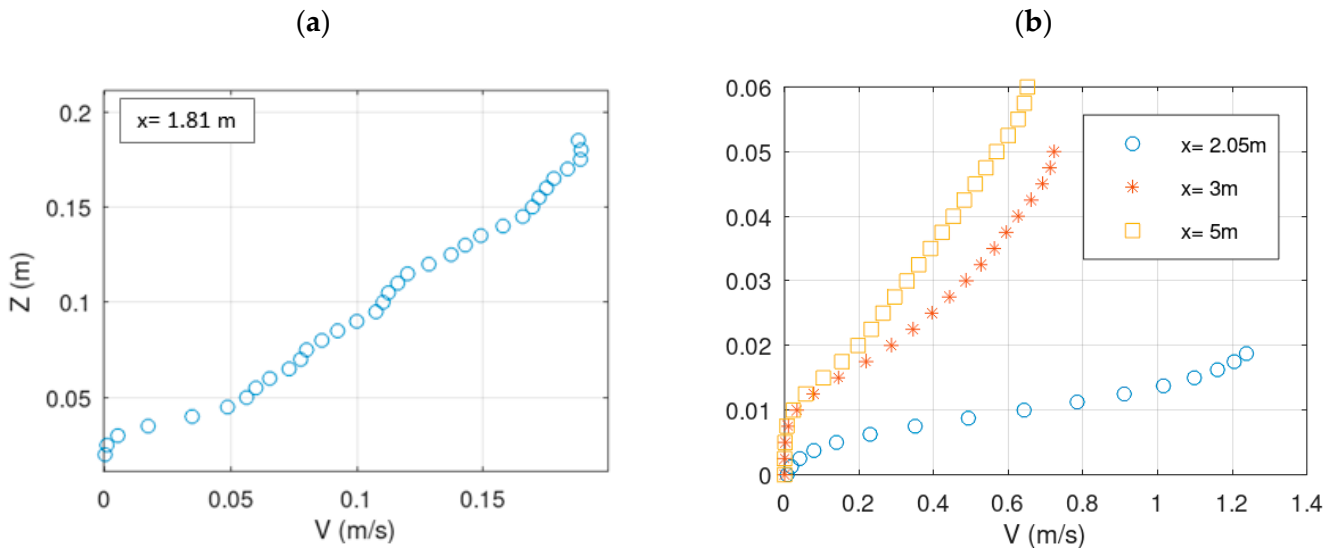


Figure 8. AVM. The velocity profiles at the selected longitudinal positions on the plane vertical mid-plane of the channel, Y = 0.075 m. (**a**) The location upstream of the sluice gate, X = 1.81 m. (**b**) The locations downstream of the sluice gate. T = 200 s, flow steady in the mean.

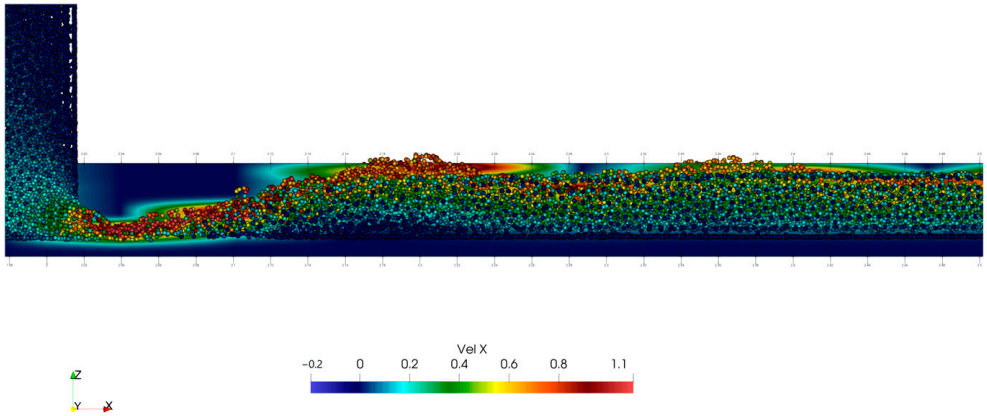


Figure 9. AVM. The side view Y = 0.075 m. Characteristics of the hydraulic jump at T = 200 s.

It should be noticed that small undulations on the free surface occurred after the jump in the SPH simulation, which was not necessarily in line with the standard description of a perfect weak jump type.

For a classical hydraulic jump, the theoretical ratio of the sequent depths (y_1, y_2) under free flow conditions is given by

$$\frac{y_2}{y_1} = \frac{1}{2}\left[-1 + \sqrt{1 + 8{Fr_1}^2}\right] \tag{19}$$

where Fr_1 is the Froude number upstream of the jump. The comparison between simulation results and the standard 1D analysis resulted in a relative difference of 6.38%. It should be noticed that this was expected since a 3D simulation with bottom and side wall friction was compared with the 1D analysis developed under strict simplifying assumptions, such as that there is no shear stress at the channel bottom for wide channels [44].

3.3.2. Laminar + SPS Turbulence Model (L-SPS)

Keeping the same hydraulic system geometry, initial and boundary conditions, and physical parameters, we conducted simulations for VB = 1, 10, and 100. The results achieved with VB = 100 are presented in this section.

In this case, the hydraulic jumps was formed at X = 2.25 m (see Figure 10). It is evident that the location where the hydraulic jump was formed was quite different from the one calculated with the AVM. The difference observed between the two models was not surprising. We believe that the observed variation in the hydraulic jump position between the two models demonstrated how differently they handle turbulence and dissipation. AVM can introduce excessive numerical dissipation into the flow field given that is an artificial dissipation term rather than a way to model physical viscosity [45]. This over-dissipation not only smooths out gradients but can also shift critical flow features, such as the hydraulic jump, away from their physically correct locations. Furthermore, in the artificial viscosity model, physical viscosity was influenced by simulation parameters like particle resolution and the speed of sound. This dependence can compromise the accuracy and consistency of the predicted hydraulic jump position.

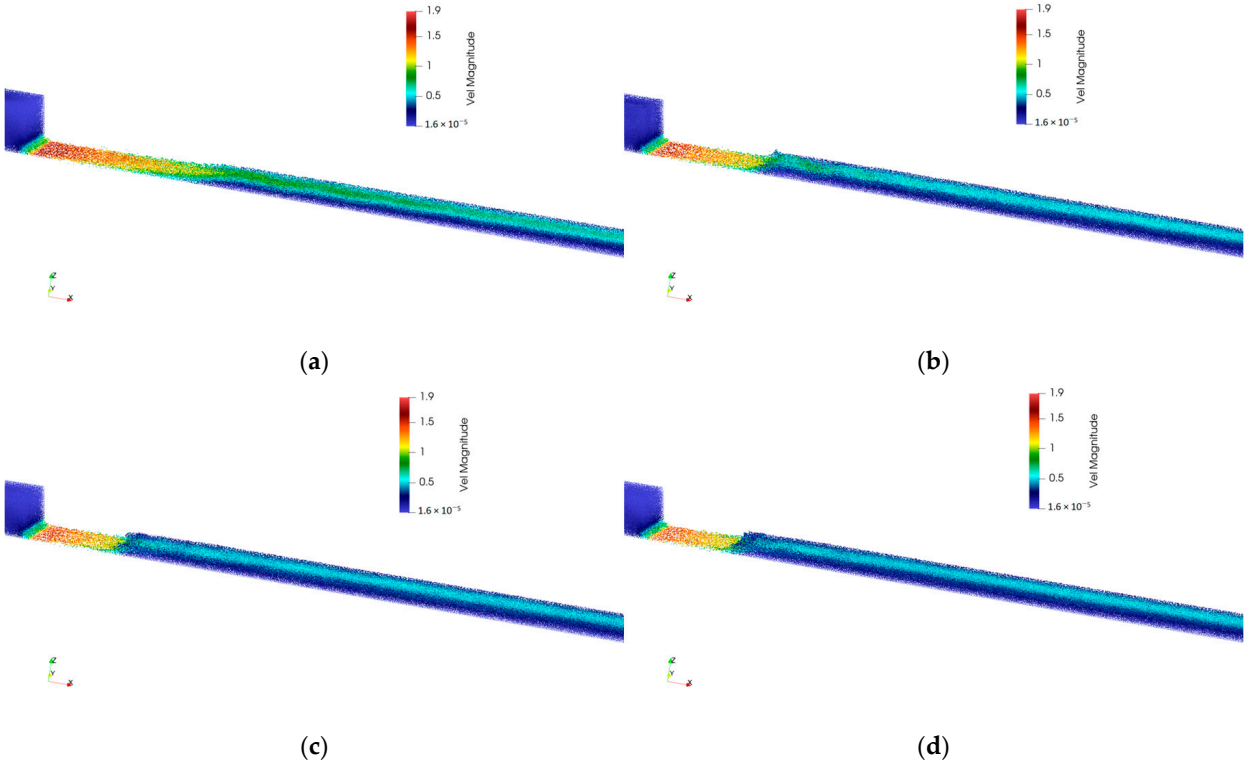


Figure 10. L-SPS. The transient formation of the hydraulic jump. (**a**) T = 50 s, (**b**) T = 100 s, (**c**) T = 150 s, (**d**) T = 200 s.

The Laminar + SPS turbulence model employed the Standard Smagorinsky LES approach. This methodology is more suited to resolving turbulent structures and capturing energy transfer across scales. Thus, L-SPS was expected to produce a more accurate prediction of the hydraulic jump location.

For these reasons, we argue that L-SPS offers a more reliable and physically consistent prediction of the hydraulic jump position.

The expected vortices upstream of the sluice gate were also formed in this case. Indeed, they appearred in an even clearer and more organized form. From Equation (18), X_v = 0.06 m, and Y_v = 0.016 m. In the L-SPS results, centers of the vortices were located at $X_{v\text{-}SPH}$ = 0.06 m (exactly as anticipated and $Y_{v\text{-}SPH}$ = 0.04 m, which deviated considerably

from the value calculated based on Equation (18)). This discrepancy may be attributed to the narrowness of the channel [42].

We also observed the appearance of secondary vortices in the flow pattern (see Figure 11). This could be a key feature in the design or the analysis of such systems. For example, the presence of secondary vortices contributes to additional turbulence in high-velocity flows. Furthermore, secondary vortices can influence sediment transport by affecting deposition and scouring patterns, which are crucial considerations for system longevity and environmental management.

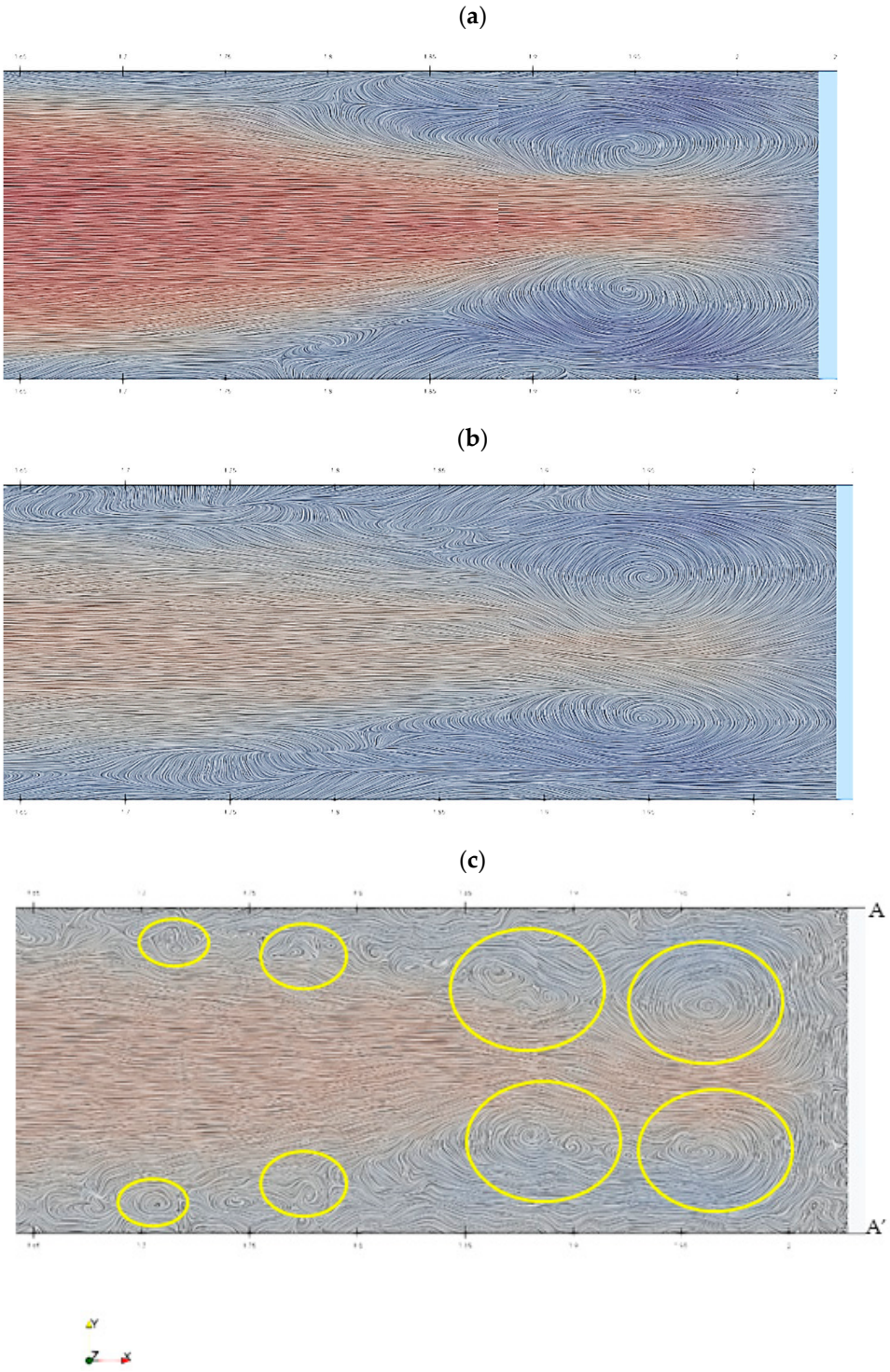


Figure 11. L-SPS. The transient formation of coherent vortices upstream of the sluice gate as seen on a horizontal plane at Z = 0.18 m, (**a**) T = 100 s, (**b**) T = 150 s, (**c**) T = 200 s. AA′ the sluice gate.

The flow was in a transient state for around 140 s. Time series plots corresponded at points upstream from the sluice gate: points A1, A2, and A3; see Figure A4. They also corresponded at points downstream from the sluice gate and beyond the influence of hydraulic jump: point B1, B2, and B3; see Figure A5. The position of each point is illustrated in Figure A3, Appendix B. Figures 12 and 13 demonstrate the color-coded velocity distribution at cross-sections X = 1.81 m and X = 3 m. The velocity distribution was as expected qualitatively in both cross-sections.

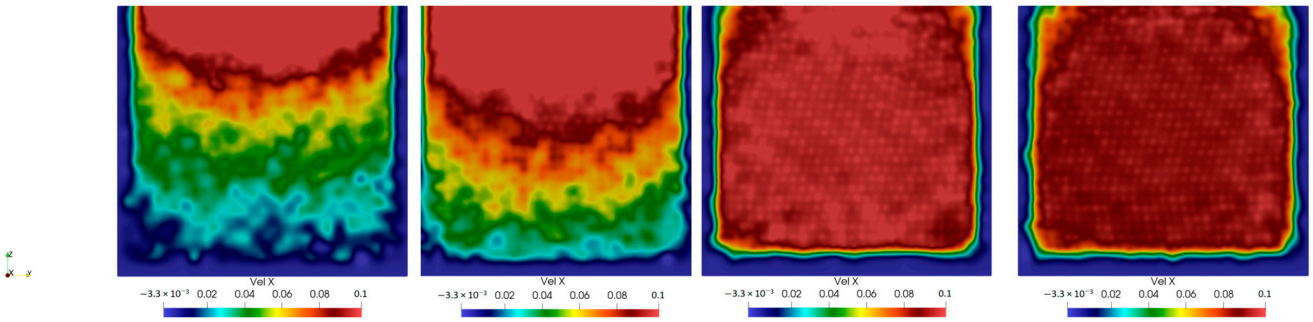


Figure 12. L-SPS. X-component of velocity. X = 1.81 m. Front view. Snapshots at T = 50, T = 100, T = 150, T = 200 s.

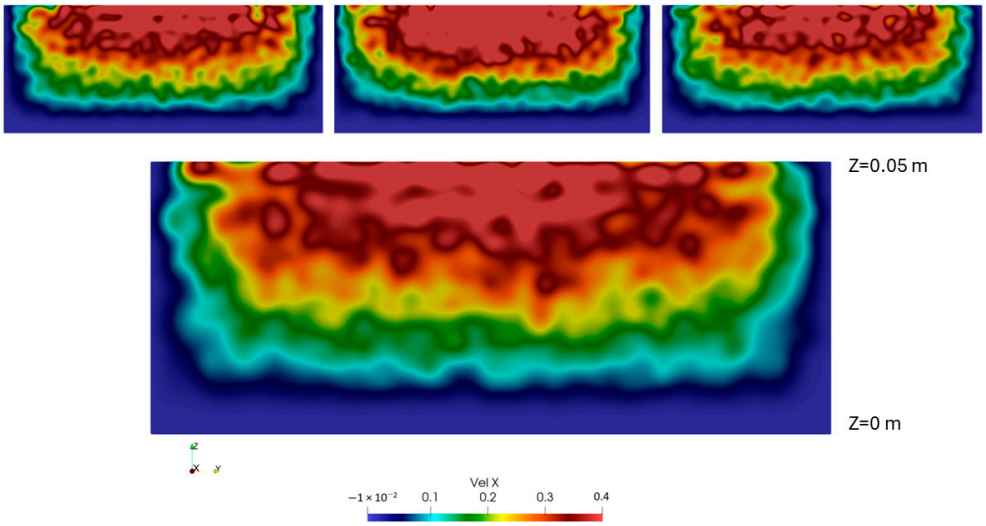


Figure 13. L-SPS. X-component of velocity at X = 3 m. Front view. Snapshots at T = 50, T = 100, T = 150, T = 200 s.

Mass conservation was satisfied as expected. The volume flow rate and the mean velocity value for each location are presented in Table 3.

Table 3. L-SPS (Q_{inlet} = 2.5 L/s). The mean velocity value and water depth at selected points. Here, h is the water depth.

V_{1_81} = 0.093 m/s	V_{2_05} = 0.96 m/s	V_3 = 0.335 m/s
h_{1_81} = 0.18 m	h_{2_05} = 0.0175 m	h_5 = 0.05 m
q_{1_81} = 0.0168 m^2/s	q_{2_05} = 0.0168 m^2/s	q_3 = 0.0168 m^2/s

Velocity profiles on channel vertical midplane (Y = 0.075 m) and at selected longitudinal locations are shown in Figure 14.

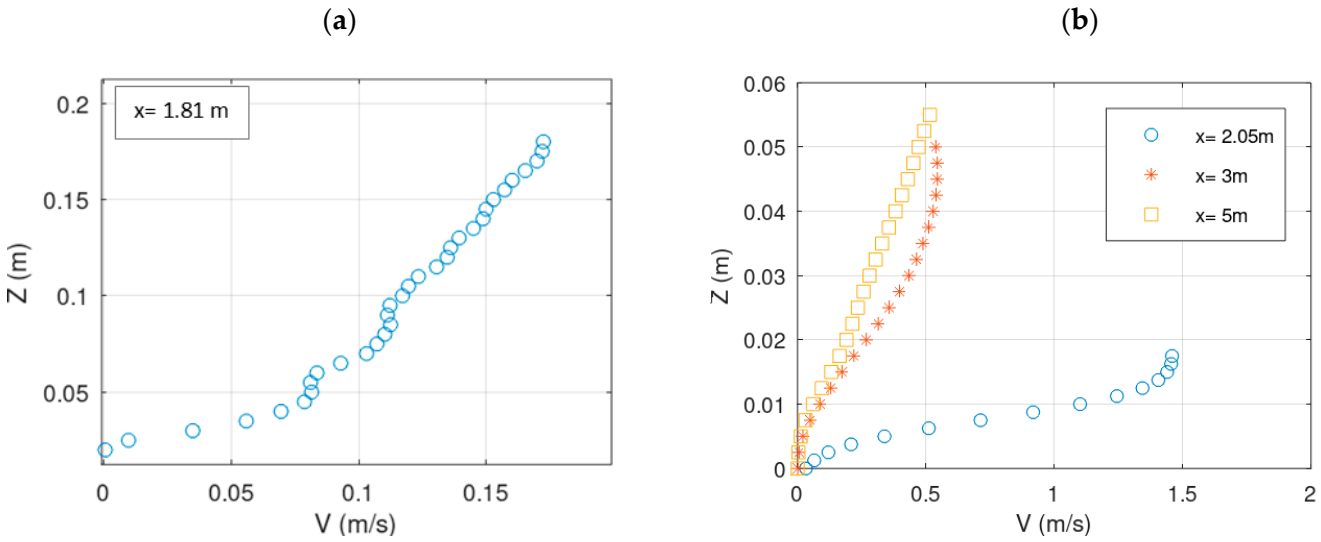


Figure 14. L-SPS. The velocity profile at selected longitudinal locations on plane Y = 0.075 m (mid vertical plane of the channel). (**a**) The position upstream of the sluice gate, X = 1.81 m, and (**b**) the positions downstream of the sluice gate. T = 200 s, steady in the mean flow.

The hydraulic jump formed at X = 2.25 m. While a series of small rollers developed on the surface, the downstream water surface remained smooth (Figure 15) with no undulation after the jump. These features categorized the jump as a weak jump type [43]. The Froude number of the jump was Fr_1 = 2.25, confirming its classification as a weak jump based on its Froude number [43]. Comparison between simulation results and the standard 1D analysis of the hydraulic jump resulted in a relative difference of 1.4%.

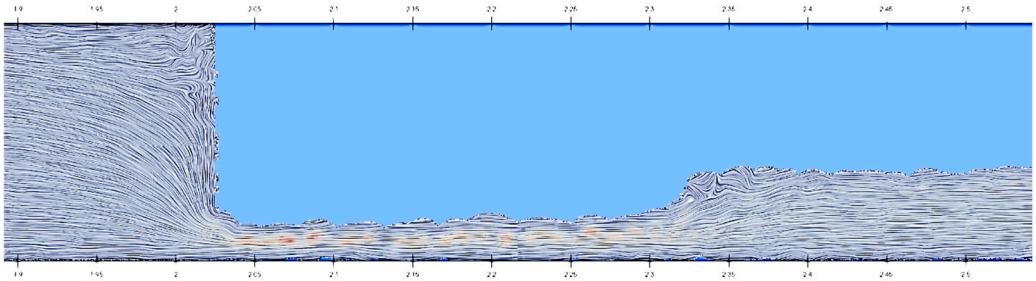


Figure 15. L-SPS. Streamlines at Y = 0.075 m (channel mid vertical plane), T = 200 s.

3.4. Comparison of the Present SPH Results with Yoosefdoost et al. Experimental Study

Yoosefdoost et al. [32] conducted a series of experiments to characterize the steady-in-the-mean flow through a sluice gate as a function of various upstream and downstream water depths. Their emphasis was on identifying conditions for free, submerged, and partially submerged flow downstream of the sluice gate as well as determining the coefficient of discharge under varying experimental conditions. The channel geometry used in their experiments is identical to that of the numerical simulations presented in this study. They tested a range of target flow rates, gate openings, and weir heights, resulting in flows that encompassed a wide array of sluice gate operating conditions, including both free and submerged hydraulic jumps. However, for the purposes of this investigation, we focused on conditions associated with free hydraulic jumps. Specifically, we simulated a flow rate of Q = 2.5 L/s with a gate opening of Y_G = 25 mm and a weir height of H_{weir} = 25 mm. The results obtained from the SPH simulations were found to be in good agreement with the experimental data reported in [32] and empirical relations [46], as can be seen in Figure 16. The case named "DBC" corresponded to a simulation that used dynamic boundary condi-

tions (DBCs) and a VB = 1. The turbulence model selected was the Laminar + SPS, while the rest of simulation parameters were constant with the previous two cases. A DBC is the default option for solid BCs treatment in the DualSPHysics code. It is based on fictious particles (as in mDBCs), first presented by Dalryble and Knio [47]. When a fluid particle approaches another one within less than distance 2 h from the boundary, the density of boundary particles increases, leading to pressure increase. This results in a repulsive force keeping fluid particles from penetrating the solid walls [48]. It is evident that the DBC case showed less satisfactory agreement with the experimental data. This was expected given that standard DBCs show limitations with density stabilization at solid boundaries, which leads to oscillations close to the solid walls [31]. The superiority of the mDBCs used in this study was apparent.

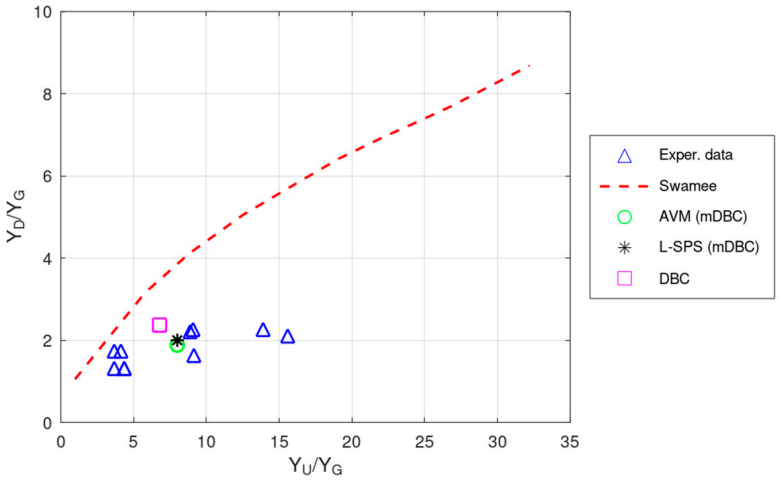


Figure 16. Comparison of SPH results with experimental data [32] and Swamee [46] empirical relations.

4. Discussion

We have examined the performance of two turbulent models for estimating dissipation in the context of the SPH method formulated as in [34,49]: artificial viscosity model and Laminar plus SPS.

In both cases, the application of modified dynamic boundary conditions (mDBCs) for the liquid/solid boundary conditions proved to be crucial for ensuring the accuracy and overall quality of the results. This is in line with previous findings, where less sophisticated boundary conditions have led to larger discrepancies when compared with experimental data (as illustrated in [18]) and previous SPH simulations [50]. In the present study, the use of mDBCs allowed for better agreement with expected physical behavior and yielded reliable results when compared with experimental data. It should be noted that these results were achieved with a relatively low spatial resolution.

The choice of the turbulence model was also a pivotal factor. It became evident that the Laminar + SPS viscosity model was the most suitable for capturing the flow dynamics under the studied conditions. Although artificial viscosity produced acceptable results, it simplified the representation of turbulence, missing the intricacies of turbulent structures. This limitation is particularly apparent in high-energy flows, where it tends to smooth out important features. On the other hand, the Laminar + SPS model, by providing a more detailed treatment of turbulence, captured effectively essential aspects of the flow coherent structures. The presence of secondary vortices in L-SPS results were either less noticeable or absent in AVM. These secondary vortices may have significant implications not only for fluid dynamics but also for the design of the flow control system. This opens new directions for research, particularly in optimizing flow behavior in applications, such as energy dissipation in hydraulic structures system sustainability and environmental management.

Finally, the hydraulic jump formation is predicted more accurately in L-SPS-based simulations. Accurate predictions on hydraulic jumps (downstream water depth, type of the jump, jump's length, etc.) can help in the designing of effective flood control systems, propose optimal gate placement to minimize downstream turbulence, and ensure a more effective design of such systems in general.

In summary, these results emphasize the importance of selecting appropriate boundary conditions and viscosity models in SPH simulations to accurately capture flow behaviors, especially in complex and turbulent systems. The combination of mDBCs with the Laminar + SPS turbulence model and the cautiously chosen "ViscoBound" parameter were critical for the successful completion of this study. These findings suggest that further robustness of boundary condition imposition and turbulence modeling could enhance the accuracy of future SPH simulations, particularly in flows characterized by complex vortical structures and significant turbulence. It is worth examining the performance of other turbulence models, e.g., the k-ε model and its extensions [51], k-ω model, dynamic Smagorinsky (LES), etc., in the context of SPH methodology in order to find a balance between accuracy and computational cost for distinct families of hydraulic problems. We believe that it is also worth developing a framework for coupling the SPH simulations of the flow in the hydraulic structure with Artificial Neural Network-based flow control systems [52].

5. Conclusions

This study presents the findings of a highly turbulent 3D flow simulation with the SPH method. It demonstrates that employing the modified dynamic boundary conditions (mDBCs) and performing parameter sensitivity analysis are key approaches to achieving accurate simulation results. Compared to simpler boundary conditions used in earlier studies, mDBCs show significantly better agreement with experimental data and theoretical predictions.

In terms of turbulence models, the Laminar + SPS proved to be the best choice for capturing turbulent flow behavior. The artificial viscosity model gave us good qualitative results, yet it fell short in accurately describing turbulent flow coherent structures.

In conclusion, this study underscores the importance of using proper boundary conditions and advanced viscosity models in SPH simulations. Not only does this improve accuracy, but it also unlocks new opportunities for both theoretical research and practical applications in fluid dynamics. In addition, the validated 3D SPH model could be used as reference data for future applications or larger scale problems.

Future research should focus on refining turbulence models and exploring the behavior of more intricate flow structures in higher resolution simulations, multi-resolution approaches, or advanced wall function approaches close to the liquid/solid interfaces. Multiphase flow modeling should also be part of an advanced simulation of hydraulic jump phenomena.

Author Contributions: Conceptualization, E.C. and A.L.; methodology, A.L.; software, E.C.; validation, E.C. and A.L.; investigation, E.C. and A.L.; resources, A.L.; data curation, E.C.; writing—original draft preparation, E.C.; writing—review, augmentation and editing, A.L.; visualization, E.C.; supervision, A.L.; project administration, A.L.; funding acquisition, A.L. All authors have read and agreed to the published version of the manuscript.

Funding: This research project was supported by the Hellenic Foundation for Research and Innovation (H.F.R.I.) under the "2nd Call for H.F.R.I. Research Projects to support Faculty Members & Researchers" (Project Number: 4584). E. Chatzoglou was supported by a doctoral candidate scholarship of the Center of Research Innovation and Excellence of the University of Thessaly, funded by the Special Account for Research Grants of the University of Thessaly.

Data Availability Statement: Data available upon request.

Conflicts of Interest: The authors declare no conflicts of interest.

Appendix A

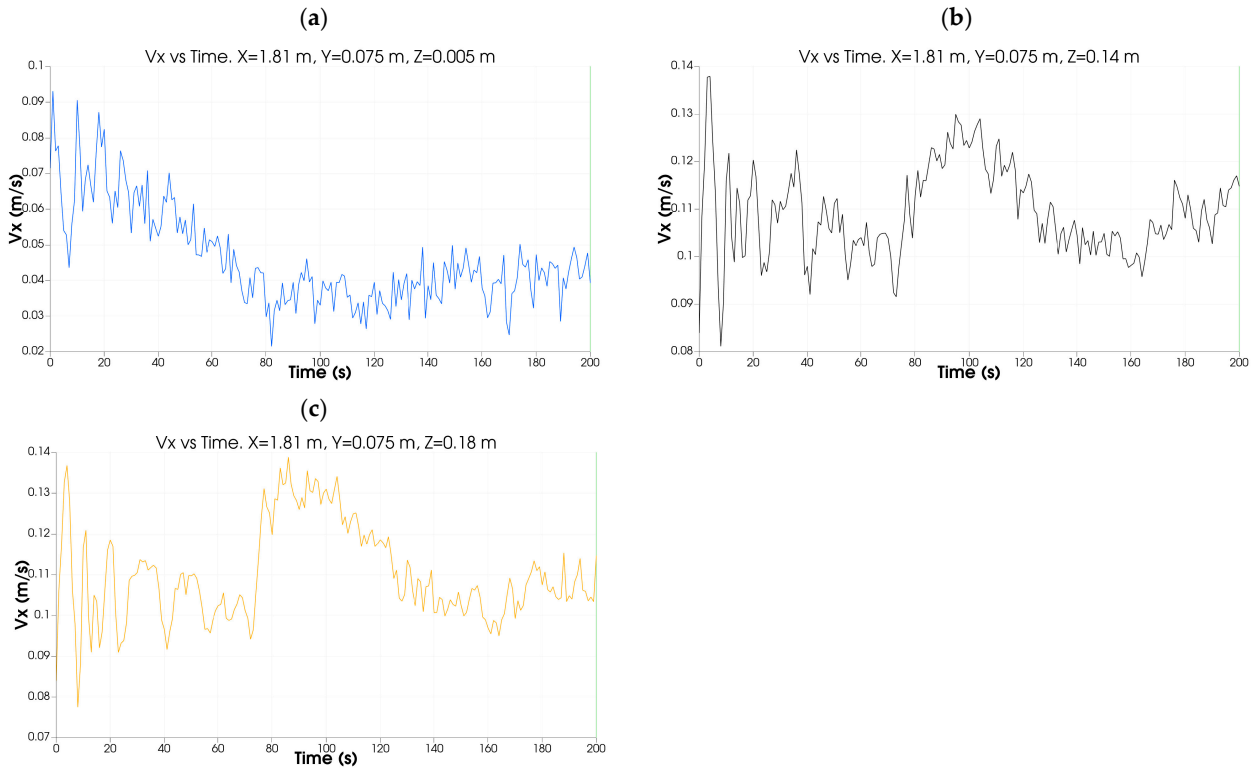


Figure A1. AVM. The time series of the X-component of velocity at X = 1.81 m (upstream of the sluice gate). (**a**) Point X = 1.81 m, Y = 0.075 m, Z = 0.005 m; (**b**) Point X = 1.81 m, Y = 0.075 m, Z = 0.14 m; (**c**) Point X = 1.81 m, Y = 0.075 m, Z = 0.18 m.

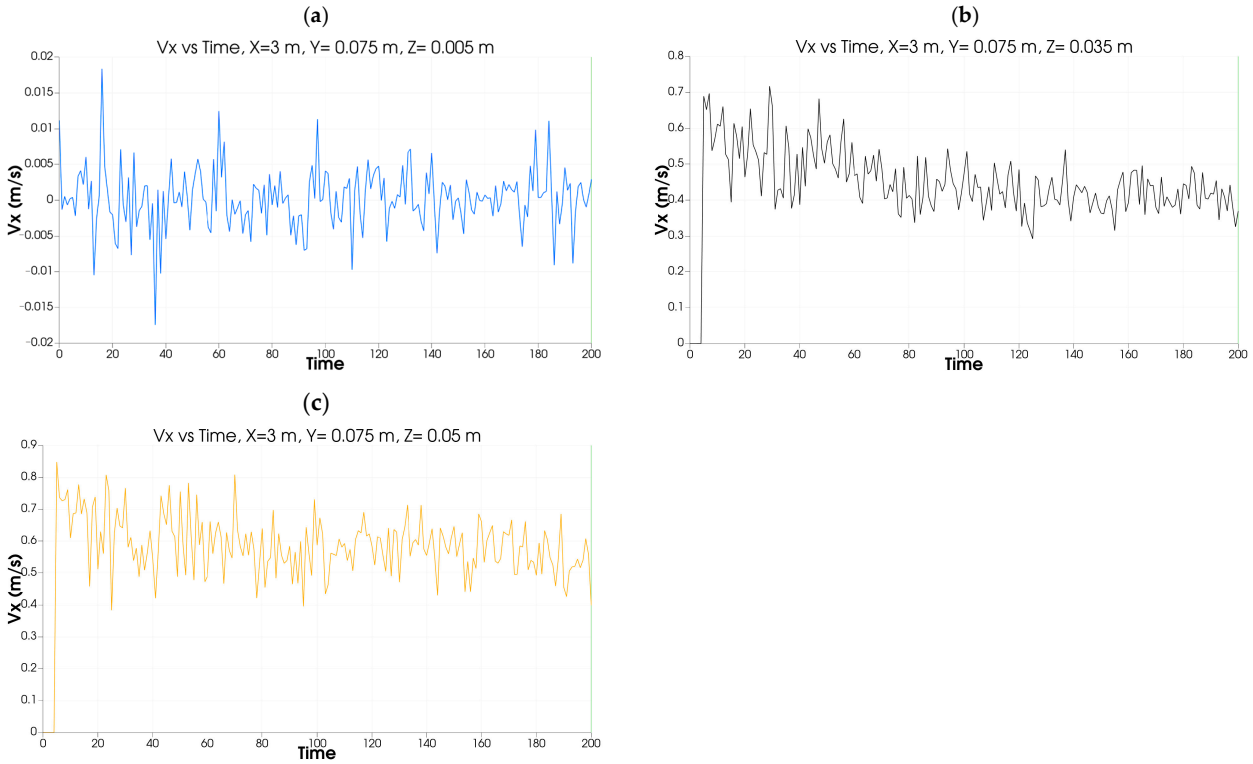


Figure A2. AVM. The time series of the X-component of velocity at X = 3 m (downstream of the hydraulic jump). (**a**) Point X = 3 m, Y = 0.075 m, Z = 0.005 m; (**b**) Point X = 3 m, Y = 0.075 m, Z = 0.035 m; (**c**) Point X = 3 m, Y = 0.075 m, Z = 0.05 m.

Appendix B

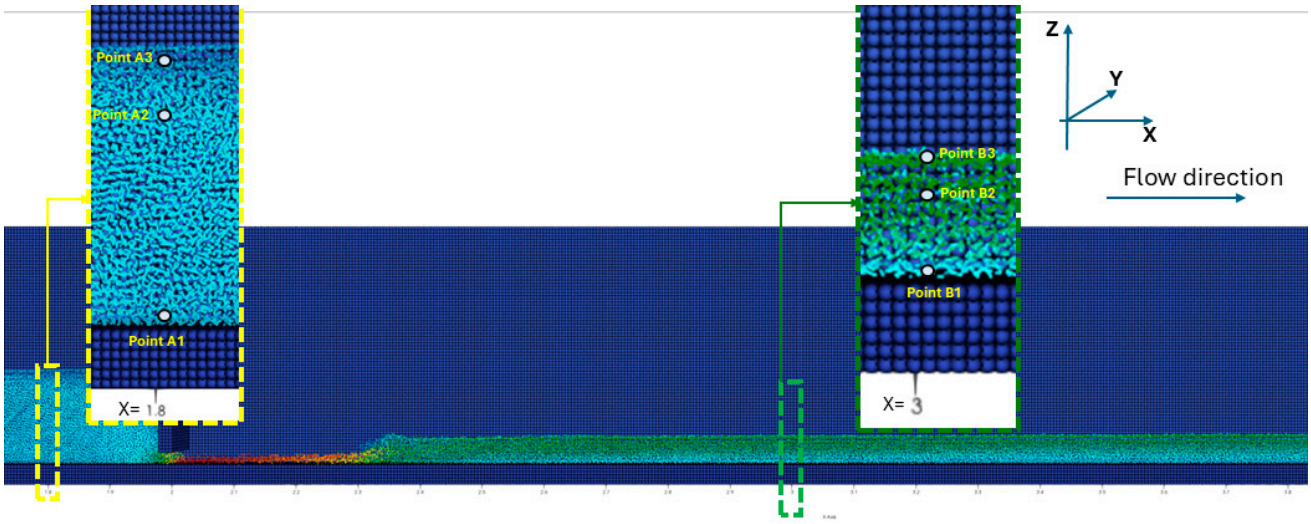


Figure A3. The visualization of L-SPS at Y = 0.075 m, showing flow characteristics on a clipped plane with projections on the channel's back wall. The locations of measurement points (A1–A3, B1–B3) at X = 1.8 m and X = 3 m are highlighted.

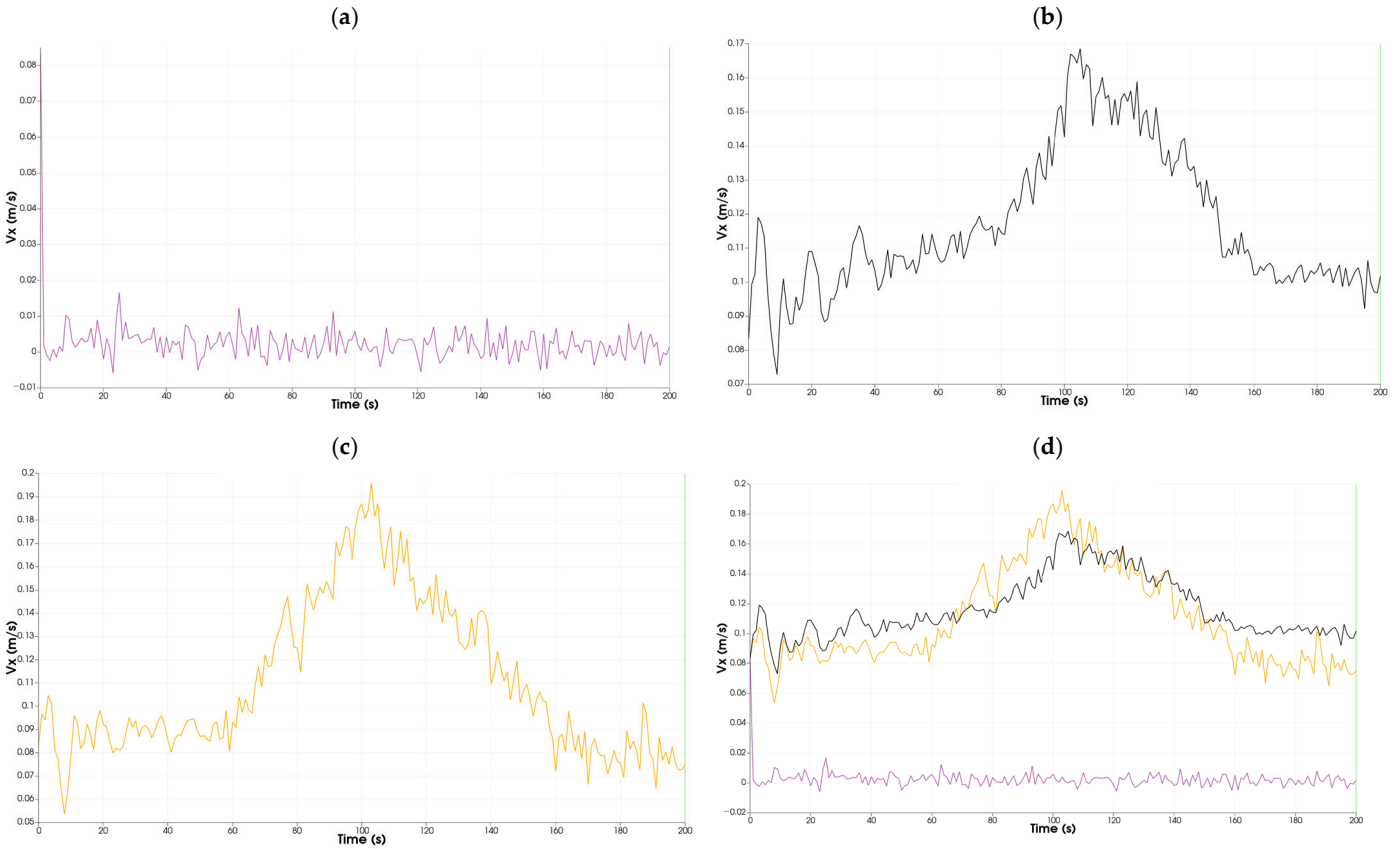


Figure A4. L-SPS. The time series of the X-component of velocity at X = 1.81 m (upstream of the sluice gate). (**a**) Point A1, X = 1.81 m, Y = 0.075 m, Z = 0.005 m; (**b**) Point A2, X = 1.81 m, Y = 0.075 m, Z = 0.14 m; (**c**) Point A3, X = 1.81 m, Y = 0.075 m, Z = 0.18 m; (**d**) all points.

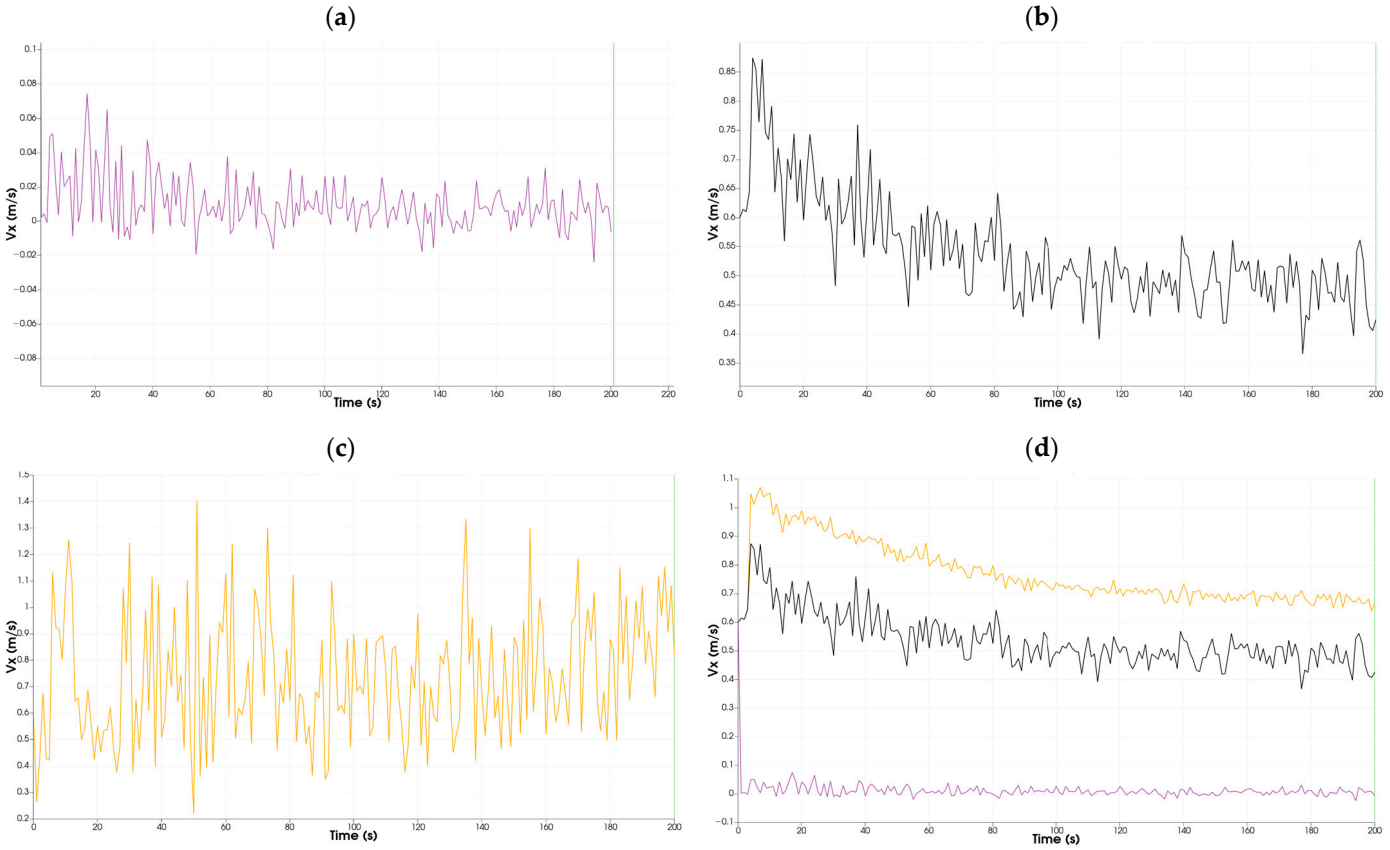


Figure A5. L-SPS. The time series of the X-component of velocity at X = 3 m (downstream of the hydraulic jump). (**a**) Point B1, X = 3 m, Y = 0.075 m, Z = 0.005 m; (**b**) Point B2, X = 3 m, Y = 0.075 m, Z = 0.035 m; (**c**) Point B3, X = 3 m, Y = 0.075 m, Z = 0.05 m; (**d**) all points.

References

1. Kubrak, E.; Kubrak, J.; Kiczko, A.; Kubrak, M. Flow Measurements Using a Sluice Gate; Analysis of Applicability. *Water* **2020**, *12*, 819. [CrossRef]
2. Shadloo, M.S.; Oger, G.; Le Touzé, D. Smoothed particle hydrodynamics method for fluid flows, towards industrial applications: Motivations, current state, and challenges. *Comput. Fluids* **2016**, *136*, 11–34. [CrossRef]
3. Mangiardi, C.M.; Ralf, M. A hybrid algorithm for parallel molecular dynamics simulations. *Comput. Phys. Commun.* **2017**, *219*, 196–208. [CrossRef]
4. Espanol, P.; Patrick, B.W. Perspective: Dissipative particle dynamics. *J. Chem. Phys.* **2017**, *146*, 150901. [CrossRef] [PubMed]
5. Ellero, M.; Español, P. Everything you always wanted to know about SDPD* (*but were afraid to ask). *Appl. Math. Mech.* **2017**, *39*, 103–124. [CrossRef]
6. Gingold, R.A.; Monaghan, J.J. Smoothed particle hydrodynamics-theory and application to non-spherical stars. *Mon. Not. Astron. Soc.* **1977**, *181*, 375–389. [CrossRef]
7. Violeau, D. *Fluid Mechanics and the SPH Method: Theory and Applications*; Oxford University Press: Oxford, UK, 2012.
8. Altomare, C.; Scandura, P.; Cáceres, I.; Viccione, G. Large-scale wave breaking over a barred beach: SPH numerical simulation and comparison with experiments. *Coast. Eng.* **2023**, *185*, 104362. [CrossRef]
9. Altomare, C.; Suzuki, T.; Domínguez, J.M.; Crespo, A.J.; Gómez-Gesteira, C.; Caceres, I. A hybrid numerical model for coastal engineering problems. In Proceedings of the 34th International Conference on Coastal Engineering (ICCE), Seoul, Republic of Korea, 15–20 June 2014. [CrossRef]
10. Lind, S.J.; Stansby, P.K.; Rogers, B.D.; Lloyd, P.M. Numerical predictions of water-air wave slam using incompressible-compressible smoothed particle hydrodynamics. *Appl. Ocean. Res.* **2015**, *49*, 57–71. [CrossRef]
11. Amaro, A.; Liang-Yee, C.; Sergei, K.B. A comparison between weakly-compressible smoothed particle hydrodynamics (WCSPH) and moving particle semi-implicit (MPS) methods for 3D dam-break flows. *Int. J. Comput. Methods* **2021**, *18*, 2050036. [CrossRef]
12. Zhu, G.X.; Zou, L.; Chen, Z.; Wang, A.; Liu, M. An improved SPH model for multiphase flows with large density ratios. *Int. J. Numer. Methods Fluids* **2018**, *86*, 167–184. [CrossRef]

13. Pozorski, J.; Olejnik, M. Smoothed particle hydrodynamics modelling of multiphase flows: An overview. *Acta Mech.* **2024**, *235*, 1685–1714. [CrossRef]
14. Mayrhofer, A.; Laurence, D.; Rogers, B.D.; Violeau, D. DNS and LES of 3-D wall-bounded turbulence using smoothed particle hydrodynamics. *Comput. Fluids* **2015**, *115*, 86–97. [CrossRef]
15. Chatzoglou, E.; Liakopoulos, A.; Sofos, F. Smoothed Particle Hydrodynamics-Based Study of 3D Confined Microflows. *Fluids* **2023**, *8*, 137. [CrossRef]
16. Alexiadis, A.; Ghraybeh, S.; Qiao, G. Natural convection and solidification of phase-change materials in circular pipes: A SPH approach. *Comput. Mater. Sci.* **2018**, *150*, 475–483. [CrossRef]
17. Sigalotti, L.D.; Alvarado-Rodríguez, G.; Aragón, F.; Álvarez Salazar, V.S.; Carvajal-Mariscal, I.; Real Ramirez, C.A.; Gonzalez-Trejo, J.; Klapp, J. SPH simulations and experimental investigation of water flow through a Venturi meter of rectangular cross-section. *Sci. Rep.* **2023**, *13*, 21215. [CrossRef] [PubMed]
18. Chatzoglou, E.; Liakopoulos, A. Flow regimes in sluice gate-weir systems: 3D SPH-based model validation. In Proceedings of the 17th International SPHERIC Workshop, Rhodes, Greece, 27–29 June 2023.
19. Zhang, J.; Wang, B.; Jiang, Q.; Hou, G.; Li, Z.; Liu, H. Numerical Study of Fluid–Solid Interaction in Elastic Sluice Based on SPH Method. *Water* **2023**, *15*, 3738. [CrossRef]
20. Martínez-Estévez, I.; Tagliafierro, B.; El Rahi, J.; Domínguez, J.M.; Crespo, A.J.; Troch, P.; Gómez-Gesteira, M. Coupling an SPH-based solver with an FEA structural solver to simulate free surface flows interacting with flexible structures. *Comput. Methods Appl. Mech. Eng.* **2023**, *410*, 115989. [CrossRef]
21. Vacondio, R.; Altomare, C.; De Leffe, M.; Hu, X.; Le Touzé, D.; Lind, S.; Souto-Iglesias, A. Grand challenges for smoothed particle hydrodynamics numerical schemes. *Comput. Part. Mech.* **2021**, *8*, 575–588. [CrossRef]
22. Monaghan, J.J. Simulating free surface flows with SPH. *J. Comput. Phys.* **1994**, *110*, 399–406. [CrossRef]
23. Monaghan, J.J.; Kajtar, J.B. SPH particle boundary forces for arbitrary boundaries. *Comput. Phys. Commun.* **2009**, *180*, 1811–1820. [CrossRef]
24. Kulasegaram, S.; Bonet, J.; Lewis, R.W.; Profit, M. A variational formulation based contact algorithm for rigid boundaries in twodimensional SPH applications. *Comput. Mech.* **2004**, *33*, 316–325. [CrossRef]
25. Leroy, A.; Violeau, D.; Ferrand, M.; Kassiotis, C. Unified semianalytical wall boundary conditions applied to 2-D incompressible SPH. *J. Comput. Phys.* **2014**, *261*, 106–129. [CrossRef]
26. Mayrhofer, A.; Rogers, B.D.; Violeau, D.; Ferrand, M. Investigation of wall bounded flows using SPH and the unified semi-analytical wall boundary conditions. *Comput. Phys. Commun.* **2013**, *184*, 2515–2527. [CrossRef]
27. Crespo, A.J.C.; Gomez-Gesteira, M.; Dalrymple, R.A. Boundary conditions generated by dynamic particles in SPH methods. *Comput. Mater. Contin.* **2007**, *5*, 173–184. [CrossRef]
28. Marrone, S.; Antuono MA, G.D.; Colagrossi, A.; Colicchio, G.; Le Touzé, D.; Graziani, G. δ-SPH model for simulating violent impact flows. *Comput. Methods Appl. Mech. Eng.* **2011**, *200*, 1526–1542. [CrossRef]
29. Adami, S.; Hu, X.Y.; Adams, N.A. A generalized wall boundary condition for smoothed particle hydrodynamics. *J. Comput. Phys.* **2012**, *231*, 7057–7075. [CrossRef]
30. Fourtakas, G.; Dominguez, J.M.; Vacondio, R.; Rogers, B.D. Local uniform stencil (LUST) boundary condition for arbitrary 3-D boundaries in parallel smoothed particle hydrodynamics (SPH) models. *Comput. Fluids* **2019**, *190*, 346–361. [CrossRef]
31. English, A.; Domínguez, J.M.; Vacondio, R.; Crespo, A.J.C.; Stansby, P.K.; Lind, S.J.; Gómez-Gesteira, M. Modified dynamic boundary conditions (mDBC) for general-purpose smoothed particle hydrodynamics (SPH): Application to tank sloshing, dam break and fish pass problems. *Comput. Part. Mech.* **2022**, *9*, 1–15. [CrossRef]
32. Yoosefdoost, M.; Lubitz, W.D. Sluice gate design and calibration: Simplified models to distinguish flow conditions and estimate discharge coefficient and flow rate. *Water* **2022**, *14*, 1215. [CrossRef]
33. Domínguez, J.M.; Fourtakas, G.; Altomare, C.; Canelas, R.B.; Tafuni, A.; García-Feal, O.; Martínez-Estévez, I.; Mokos, A.; Vacondio, R.; Crespo, A.J.C.; et al. DualSPHysics: From fluid dynamics to multiphysics problems. *Comput. Part. Mech.* **2022**, *9*, 867–895. [CrossRef]
34. Monaghan, J.J. Smoothed particle hydrodynamics. *Annu. Rev. Astron. Astrophys.* **1992**, *30*, 543–574. [CrossRef]
35. Liu, G.R. *Mesh Free Methods: Moving Beyond the Finite Element Method*; CRC Press: Boca Raton, FL, USA, 2003.
36. Monaghan, J.J. Smoothed Particle Hydrodynamics. *Rep. Prog. Phys.* **2005**, *68*, 1703–1759. [CrossRef]
37. Wendland, H. Piecewiese polynomial, positive definite and compactly supported radial functions of minimal degree. *Adv. Comput. Math.* **1995**, *4*, 389–396. [CrossRef]
38. Altomare, C.; Crespo, A.J.; Domínguez, J.M.; Gómez-Gesteira, M.; Suzuki, T.; Verwaest, T. Applicability of Smoothed Particle Hydrodynamics for estimation of sea wave impact on coastal structures. *Coast. Eng.* **2015**, *96*, 1–12. [CrossRef]
39. Dalrymple, R.A.; Rogers, B.D. Numerical modeling of water waves with the SPH method. *Coast. Eng.* **2006**, *53*, 141–147. [CrossRef]
40. Tafuni, A.; Dominguez, J.M.; Vacondio, R.; Crespo, A.J.C. A versatile algorithm for the treatment of open boundary conditions in Smoothed particle hydrodynamics GPU models. *Comput. Methods Appl. Mech. Eng.* **2018**, *342*, 604–624. [CrossRef]

41. Liu, M.B.; Liu, G.R. Restoring particle consistency in smoothed particle hydrodynamics. *Appl. Numer. Math.* **2006**, *56*, 19–36. [CrossRef]
42. Roth, A.; Hager, W.H. Underflow of standard sluice gate. *Exp. Fluids* **1999**, *27*, 339–350. [CrossRef]
43. Chaudhry, M. *Open-Channel Flow*; Prentice-Hall: Englewood Cliffs, NJ, USA, 1993.
44. Liakopoulos, A. *Hydraulics*, 3rd ed.; Tziolas Publications: Thessaloniki, Greece, 2020.
45. Basa, M.; Quinlan, N.J.; Lastiwka, M. Robustness and accuracy of SPH formulations for viscous flow. *Int. J. Numer. Methods Fluids* **2009**, *60*, 1127–1148. [CrossRef]
46. Swamee, P. Sluice-Gate Discharge Equations. *J. Irrig. Drain. Eng.* **1992**, *118*, 56–60. [CrossRef]
47. Dalrymple, A.; Knio, O. SPH modelling of water waves. *Coast. Dyn.* **2001**, *1*, 779–787.
48. Liu, S.; Ioan, N.; Majid, M. Evaluation of the solid boundary treatment methods in SPH. *Int. J. Ocean Coast. Eng.* **2018**, *1*, 1840002. [CrossRef]
49. Gotoh, H.; Shao, S.; Memita, T. SPH-LES model for numerical investigation of wave interaction with partially immersed breakwater. *Coast. Eng. J.* **2001**, *46*, 39–63. [CrossRef]
50. Chatzoglou, E.; Liakopoulos, A. Hydraulic jump simulation via Smoothed Particle Hydrodynamics: A critical review. In Proceedings of the 39th IAHR World Congress, Granada, Spain, 19–24 June 2022.
51. Liakopoulos, A. Computation of high speed turbulent boundary-layer flows using The k-ε turbulence model. *Int. J. Numer. Methods Fluids* **1985**, *5*, 81–97. [CrossRef]
52. Sahan, R.A.; Albin, D.C.; Sahan, N.K.; Liakopoulos, A. Artificial Neural Network-Based Low-Order Dynamical Modeling and Intelligent Control of Transitional Flow Systems. In Proceedings of the Sixth IEEE Conference on Control Applications, Hartford, CT, USA, 5–7 October 1997.

Disclaimer/Publisher's Note: The statements, opinions and data contained in all publications are solely those of the individual author(s) and contributor(s) and not of MDPI and/or the editor(s). MDPI and/or the editor(s) disclaim responsibility for any injury to people or property resulting from any ideas, methods, instructions or products referred to in the content.